Solar Phys (2011) 274:361–377
DOI 10.1007/s11207-010-9698-x

Global MHD Modeling of the Solar Corona and Inner Heliosphere for the Whole Heliosphere Interval

P. Riley · R. Lionello · J.A. Linker · Z. Mikic · J. Luhmann · J. Wijaya

Received: 14 October 2010 / Accepted: 3 December 2010 / Published online: 5 February 2011

Abstract In an effort to understand the three-dimensional structure of the solar corona and inner heliosphere during the Whole Heliosphere Interval (WHI), we have developed a global magnetohydrodynamics (MHD) solution for Carrington rotation (CR) 2068. Our model, which includes energy-transport processes, such as coronal heating, conduction of heat parallel to the magnetic field, radiative losses, and the effects of Alfvén waves, is capable of producing significantly better estimates of the plasma temperature and density in the corona than have been possible in the past. With such a model, we can compute emission in extreme ultraviolet (EUV) and X-ray wavelengths, as well as scattering in polarized white light. Additionally, from our heliospheric solutions, we can deduce magnetic-field and plasma parameters along specific spacecraft trajectories. In this paper, we present a general analysis of the large-scale structure of the solar corona and inner heliosphere during WHI, focusing, in particular, on *i*) helmet-streamer structure; *ii*) the location of the heliospheric current sheet; and *iii*) the geometry of corotating interaction regions. We also compare model results with *i*) EUV observations from the EIT instrument onboard SOHO; and *ii*) *in-situ* measurements

The Sun – Earth Connection near Solar Minimum
Guest Editors: M.M. Bisi, B.A. Emery, and B.J. Thompson

P. Riley (✉) · R. Lionello · J.A. Linker · Z. Mikic · J. Wijaya
Predictive Science, Inc., 9990 Mesa Rim Road, Suite 170, San Diego, CA 92121, USA
e-mail: pete@predsci.com

R. Lionello
e-mail: lionel@predsci.com

J.A. Linker
e-mail: linkerj@predsci.com

Z. Mikic
e-mail: mikicz@predsci.com

J. Wijaya
e-mail: wijayaj@predsci.com

J. Luhmann
Space Sciences Laboratory, University of California, Berkeley, CA 94720, USA
e-mail: jgluhman@ssl.berkeley.edu

made by the STEREO-A and B spacecraft. Finally, we contrast the global structure of the corona and inner heliosphere during WHI with its structure during the Whole Sun Month (WSM) interval. Overall, our model reproduces the essential features of the observations; however, many discrepancies are present. We discuss several likely causes for them and suggest how model predictions may be improved in the future.

Keywords Sun · Corona · Corotating interaction regions · Magnetic fields · Solar wind · Interplanetary medium

1. Introduction

The Whole Heliosphere Interval (WHI), which ran from 20 March through 16 April 2008, and coincided with Carrington rotation (CR) 2068, is providing a unique opportunity for both observers and modelers to collaborate in an effort to understand the three-dimensional (3D) structure and evolution of the solar corona and inner heliosphere. It builds on the previous Whole Sun Month (WSM) interval, which proved to be exceptionally successful (*e.g.*, Gibson *et al.*, 1999; Linker *et al.*, 1999; Riley *et al.*, 1999). The WHI occurred on the way to the most recent solar minimum (December 2008), which has, thus far, been unique in a number of ways. For example, in 2009 260 days (71%) were spotless. Moreover, from 1 January 2004 through 8 October 2010, 812 days have been spotless (see http://spaceweather.com), making the current solar minimum the most prolonged and quiet in a century (Phillips, 2009). The polar photospheric flux has decreased by $\approx$40% (Svalgaard and Cliver, 2007) and the coronal holes are noticeably smaller (Kirk *et al.*, 2009). Measurements by *in-situ* spacecraft show substantial differences between the recent minimum and the previous three. *Ulysses* polar observations through late 2008, in particular, suggest that *i*) the interplanetary magnetic field (IMF) was $\approx$36% lower than the previous minimum (Smith and Balogh, 2008); *ii*) the scaled number density was $\approx$17% lower (Issautier *et al.*, 2008; McComas *et al.*, 2008); and *iii*) the scaled temperature was $\approx$14% lower (McComas *et al.*, 2008). It was also determined that the bulk solar-wind speed was $\approx$3% lower, although this may not be a statistically significant change. From these measurements it was inferred that *i*) the dynamic pressure decreased by $\approx$22%; *ii*) the proton thermal pressure decreased by $\approx$25%; and *iii*) the magnetic pressure decreased by $\approx$87% (McComas *et al.*, 2008). The profiles of high-speed streams upstream of Earth also seem to be unique, being stronger, longer in duration, and more recurrent than during the previous minimum (Gibson *et al.*, 2009). Strong periodicities were also found in early-mid 2008, with periods of 9, 13.5, and 27 days (Emery *et al.*, 2008), with no comparable patterns found during the previous minimum. It appears that the solar wind at Earth during this minimum was 47% less dense and 13% faster, and the IMF is reduced by 11% (Gibson *et al.*, 2009). However, given the complexity of in-Ecliptic measurements, including the contribution from multiple sources of solar wind and the formation and evolution of compression and rarefaction regions, the causes of such changes are more difficult to interpret than the *Ulysses* polar counterparts. However, their consequences could be readily seen within the Earth's magnetosphere, particularly in the form of enhanced auroral power and an elevated radiation environment (Gibson *et al.*, 2009).

To understand the properties and structure of the corona and inner heliosphere during WHI, we can analyze a range of phenomena in remote-sensing observations and *in-situ* measurements and compare with model results. Previously, we have compared high-latitude, quiescent observations by *Ulysses* with 1D, thermodynamic solutions to understand the

acceleration characteristics of the solar wind and the relationship between magnetic-field strength within coronal holes and heating of the solar wind plasma (Riley *et al.*, 2010b). In this study, we provide a broad overview of the 3D structure of the inner heliosphere during WHI. We compare the state of the corona and heliosphere during WHI and WSM. We also directly compare model results with emission observations and *in-situ* measurements to illustrate where the model performs well and where it performs poorly. Finally, we discuss the current limitations of global magnetohydrodynamic (MHD) models and suggest from where future improvements may come.

From a global perspective of the heliosphere, two particularly useful structures are *i*) helmet streamers and *ii*) the heliospheric current sheet (HCS). Helmet streamers are arch-like, bright features seen in white-light observations. They extend outward several solar radii from the Sun and are drawn into a cusp-like structure. They are composed of closed magnetic loops that sometimes overlay sunspots and active regions (ARs). Often a prominence (or filament) is embedded at the bottom of the streamer. A necessary requirement for such loops is a neutral line (that is, the location where B_r changes sign), and the footpoints of the helmet streamer field lines lie in regions of opposite polarity. From this, we can understand the association of streamers with ARs, which contain a strong, localized neutral line, as well as their interplanetary extension in the form of stalks and association with the HCS. At solar minimum, even in the absence of any ARs, helmet streamers are produced from the large-scale solar dipole. In this case, the neutral line is a simple curve, circumscribing the Sun and confined to low heliographic latitudes. Whereas helmet streamers separate open field lines of opposite polarity, a second class of "pseudostreamers" separate field lines of the same polarity (Wang, Sheeley, and Rich, 2007). Stated another way, while helmet streamers separate coronal holes of opposite polarity, pseudostreamers separate holes of the same polarity. Wang, Sheeley, and Rich (2007) showed that although pseudostreamers also have plasma-sheet extensions, they are not associated with the HCS. As we will show, their presence during the recent minimum led to the disappearance of the more usual quiescent equatorial streamer belt.

The HCS, a surface separating regions of opposite magnetic polarity, is a fundamental feature of the heliosphere, and is intimately related to the large-scale dynamic flow of the solar wind. As the largest coherent structure within the heliosphere, the HCS acts as a "frame" about which corotating interaction regions (CIRs) are organized (Pizzo and Gosling, 1994). This makes it a particularly attractive entity to study with global MHD models (Riley, Linker, and Mikić, 2002). Its shape also plays an important role in the modulation of galactic cosmic rays (*e.g.*, Jokipii, Sonett, and Giampapa, 1997). The tilt of the HCS (that is, its maximum latitudinal extent) has displayed some unusual properties during the recent solar minimum. At the end of Cycles 21 (1986) and 22 (1996), the tilt in both hemispheres declined relatively monotonically, reaching near-zero values at approximately the same time as the sunspot number. Applying a similar relationship during the declining phase of Cycle 23, one might have predicted that the tilt of the HCS would reach zero in late 2007. However, since mid-2006 and through 2008 it remained steady at $\approx 15^\circ$ (see Figure 1).

2. Observations During WHI

Observations during WHI are discussed in several complementary companion studies (Bisi, Emery, and Thompson, 2011). Here we limit ourselves to brief remarks that will be relevant for our discussion of the model results later. To orient ourselves, in Figure 1 we summarize several solar-related time-series parameters over a period of more than three decades.

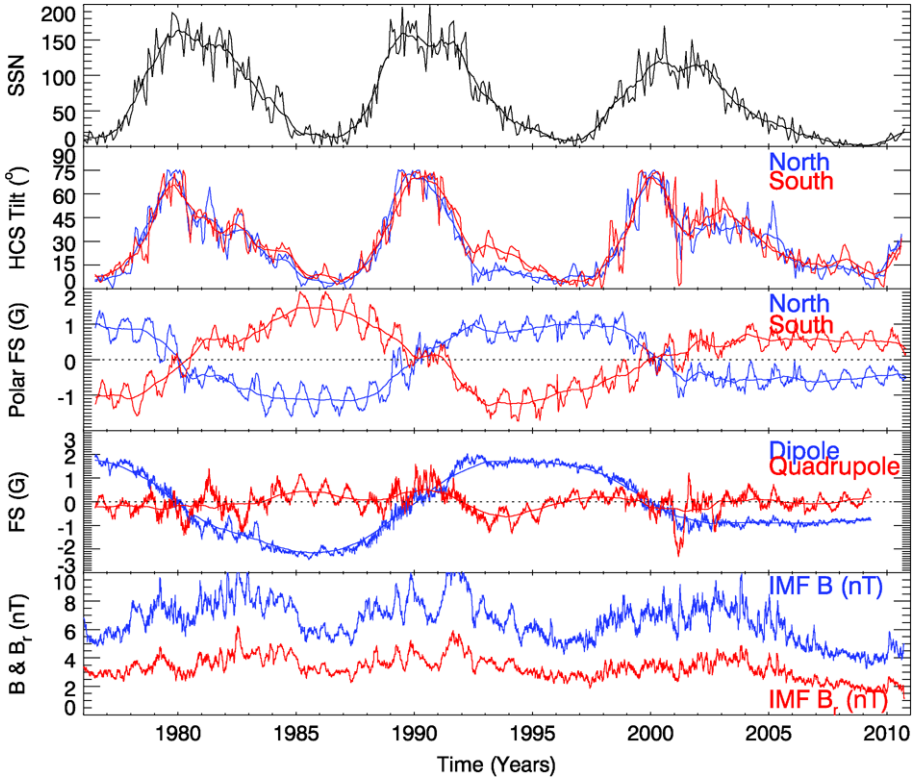

Figure 1 Time series of (a) sunspot number (SSN); (b) HCS tilt, as inferred from potential field source surface (PFSS) solutions driven by Wilcox Solar Observatory (WSO) data; (c) northern and southern polar field strengths (FS); (d) axial dipole and zonal quadrupole contributions to the field strength; and (e) total and radial IMF, as measured by the many spacecraft contributing to the OMNI dataset. Data for panels two through four were provided by J.T. Hoeksema.

We note the following points. First, the last full solar cycle (23), which spanned from August/September 1996 through December 2008 (as determined from a 12-month smoothed sunspot number (SSN): *i*) contained a more modest peak than the previous two cycles; and *ii*) lasted $\approx$2.5 years longer. Second, following the peak, the tilt (or maximum extent) of the HCS remained elevated ($\approx 45°$) for $\approx$three years, falling lower to $\approx 15°$ and again holding steady before dropping to nearly zero in 2009. Third, the polar fields have remained steady and reasonably symmetric since 2003, but at approximately half their values of the previous cycle. Fourth, following solar maximum in 2001, the quadrupolar component of the field has remained zero, while the axial-dipole component has remained relatively steady (again at half the amplitude of the previous cycles). Fifth, both the total magnitude and radial component of the IMF decreased relatively monotonically from 2003 onwards, reaching a minimum in 2009. Based on data available for 2010, activity appears to be returning: SSN is increasing, the tilt of the HCS is becoming larger, and the strength of the IMF is growing.

3. MHD Modeling of the Corona and Inner Heliosphere

MHD models have proven very successful in interpreting and comprehending a wide array of solar and heliospheric phenomena. They provide a global context for connecting diverse datasets and understanding the physical interrelationship between often dissimilar phenomena.

The first MHD models of the solar corona were developed almost 40 years ago (Endler, 1971; Pneuman and Kopp, 1971). Over the years they have become progressively more sophisticated (*e.g.*, Mikić and Linker, 1994), culminating in models that include the photospheric field as a boundary condition (*e.g.*, Riley, Linker, and Mikić, 2001; Roussev *et al.*, 2003). Complementary efforts focusing on heliospheric models, where the inner boundary was placed beyond the outermost critical point, were also pursued (*e.g.*, Pizzo, 1978; Odstrcil, 1994). Most recently, coronal and heliospheric models have been coupled (*e.g.*, Riley, Mikić, and Linker, 2003; Odstrcil *et al.*, 2004; Manchester *et al.*, 2006; Riley *et al.*, 2007), and more sophisticated descriptions of energy-transport processes have been included (*e.g.*, Lionello, Linker, and Mikić, 2009).

Our group has studied the properties of the ambient solar wind for a number of years (Riley *et al.*, 1996, 2001; Riley, Linker, and Mikić, 2001, 2002; Riley, Mikić, and Linker, 2003; Riley, 2007b), finding that, in general, our models can reproduce the essential large-scale features of the solar wind. We say "models" and not "model" because we have found that different approaches are required depending on the specific scientific question being addressed. In the simulations described here, the two primary models are *i*) the thermodynamic coronal model and *ii*) the polytropic heliospheric model. For the latter, we drive the inner radial boundary using one of two approaches: (a) directly using output from the thermodynamic coronal solution, or (b) using empirically based boundary conditions derived from the structure of the coronal magnetic field (Riley, Linker, and Mikić, 2001). In the following sections, we summarize how these models differ and justify when and how each should be applied.

3.1. The General MHD Model

In general, our 3D, time-dependent algorithm (Magnetohydrodynamics Around a Sphere: MAS) solves the following form of the resistive MHD equations on a nonuniform grid in spherical coordinates:

$$\nabla \times \mathbf{B} = \frac{4\pi}{c}\mathbf{J}, \tag{1}$$

$$\nabla \times \mathbf{E} = -\frac{1}{c}\frac{\partial \mathbf{B}}{\partial t}, \tag{2}$$

$$\mathbf{E} + \frac{\mathbf{v} \times \mathbf{B}}{c} = \eta \mathbf{J}, \tag{3}$$

$$\frac{\partial \rho}{\partial t} + \nabla \cdot (\rho \mathbf{v}) = 0, \tag{4}$$

$$\frac{1}{\gamma - 1}\left(\frac{\partial T}{\partial t} + \mathbf{v} \cdot \nabla T\right) = -T \nabla \cdot \mathbf{v} + \frac{m_{\mathrm{p}}}{2k\rho} S, \tag{5}$$

$$\rho\left(\frac{\partial \mathbf{v}}{\partial t} + \mathbf{v} \cdot \nabla \mathbf{v}\right) = \frac{1}{c}\mathbf{J} \times \mathbf{B} - \nabla(p + p_{\mathrm{w}}) + \rho \mathbf{g} + \nabla \cdot (\nu \rho \nabla \mathbf{v}), \tag{6}$$

$$S = \left(-\nabla \cdot \mathbf{q} - n_{\mathrm{e}} n_{\mathrm{p}} Q(T) + H_{\mathrm{ch}}\right); \tag{7}$$

where **B** is the magnetic field, **J** is the electric-current density, **E** is the electric field, ρ, **v**, p, and T are the plasma mass density, velocity, pressure, and temperature, respectively, $\mathbf{g} = -g_0 R_\odot^2 \hat{\mathbf{r}}/r^2$ is the gravitational acceleration, η the resistivity, and ν is the kinematic viscosity. Equation (7) contains the radiation loss function $[Q(T)]$ as in Athay (1986), n_e and n_p are the electron and proton number density (which are equal for a hydrogen plasma), m_p is the proton mass, $\gamma = 5/3$ is the polytropic index, H_{ch} is the coronal heating term, and **q** is the heat flux. A combination of Spitzer collisional ($r < 10R_\odot$) and collisionless ($r > 10R_\odot$, Hollweg, 1978) heat fluxes is used to prescribe **q**. The wave pressure term $[p_w]$ in Equation (6) represents the contribution due to Alfvén waves (Jacques, 1977) and is evolved using the Wentzel – Kramers – Brillouin (WKB) approximation for time – space averaged Alfvén wave energy density $[\epsilon]$ (Mikić *et al.*, 1999). The method of solution of Equations (1) through (6), including the boundary conditions, has been described previously (see Lionello, Linker, and Mikić, 2009 and references therein).

In the energy Equation (7), S includes radiation, thermal conduction, coronal heating, and resistive and viscous diffusion. Lionello, Linker, and Mikić (2001) describe how we incorporate these processes so as to include the upper chromosphere and transition region in the domain of the calculation. Although we simplify these equations for the heliospheric solutions by employing a "polytropic" energy equation, where $S = 0$, (*e.g.*, Linker *et al.*, 1999; Mikić *et al.*, 1999; Riley, Linker, and Mikić, 2001; Roussev *et al.*, 2003), to more accurately compute densities and temperatures in the corona (and hence the heliosphere), we prescribe a functional form for S, allowing us to set γ to a realistic value of 5/3. We refer to this model as the "thermodynamic" model, because it incorporates energy-transport processes. With such a model we can make meaningful comparisons between simulated emission (EUV and soft X-ray) and observations, which provide strong constraints on the free parameters in the heating model (Lionello, Linker, and Mikić, 2009).

Finally, an important feature that makes our approach unique is the use of observed photospheric magnetograms to drive the model. This allows us to model the specific properties of time periods of interest, including WHI and WSM.

3.2. The Heliospheric MHD Model

For computing heliospheric solutions, we have developed two complementary approaches. In the simpler empirically based technique, we use the structure of the coronal magnetic field to derive the radial velocity boundary condition at the inner edge of the heliospheric model (Riley, Linker, and Mikić, 2001). The heliospheric solutions are molded by dynamic forces so that the profile of the radial velocity at the inner boundary is believed to have the largest effect on the resulting solutions (Riley and McComas, 2009). The technique is based on the idea, supported by both the "interchange reconnection" model of L. Fisk and colleagues (Fisk, 1996; Fisk, Schwadron, and Zurbuchen, 1998) as well as the "expansion factor" models of Y.-M. Wang and colleagues (Wang and Sheeley, 1990; Cranmer, van Ballegooijen, and Edgar, 2007; Cranmer *et al.*, 2010), that the slow solar wind originates at the boundary between open and closed field lines, and the fast solar wind originates from everywhere else (that is, from deeper within coronal holes). We also use the computed magnetic field from the coronal solution directly, and infer the remaining plasma quantities (density and temperature) by assuming momentum-flux conservation and thermal-pressure balance over the sphere defining the inner boundary of the heliospheric model at $30R_\odot$.

The second, more self-consistent, approach is to drive the heliospheric model directly using all of the magnetic and plasma variables computed in the coronal solution. While this

should, in principle, be more accurate, we have found that the empirically based solutions tend to more closely match *in-situ* measurements (speed, density, temperature, and polarity of the IMF) at Earth and *Ulysses*. Ultimately, of course, we expect that as the physics contained within the coronal model improves, and the remaining free parameters become better constrained, the quality of the self-consistently derived heliospheric solutions will surpass the empirically based results. In this study, we present results using both approaches.

4. Model Results

4.1. Introduction

We computed preliminary thermodynamic solutions for both WSM and WHI. Figure 2 summarizes the large-scale structure of the inner heliosphere during these two periods. The two panels show meridional slices of the radial velocity and radial magnetic-field strength (scaled to 1 AU) in arbitrary planes, as well as an equatorial slice of the plasma density, again scaled by $1/r^2$ to values at 1 AU. Contrasting the two solutions, we note several points. First, the unipolar fields between WSM and WHI have reversed. The large-scale dipolar component of the solar field during the previous minimum (WSM) was outward over the poles of the northern hemisphere and inward over the southern poles. During WHI, which represents the minimum of the most recent cycle, it is reversed. Second, the "band of solar-wind variability," that is, the volume of the heliosphere that is defined by slower, but more variable solar wind, is narrower during WSM than during WHI. Third, this band contained several near-equatorial coronal holes that were the source of higher-speed solar wind, making the solar wind speed measured in the ecliptic plane by the *Advanced Composition Explorer* (ACE) and *Wind* more variable and complex during WHI (Gibson *et al.*, 2009). Fourth, the average number density of the solar wind during WHI was less than during WSM, yet the

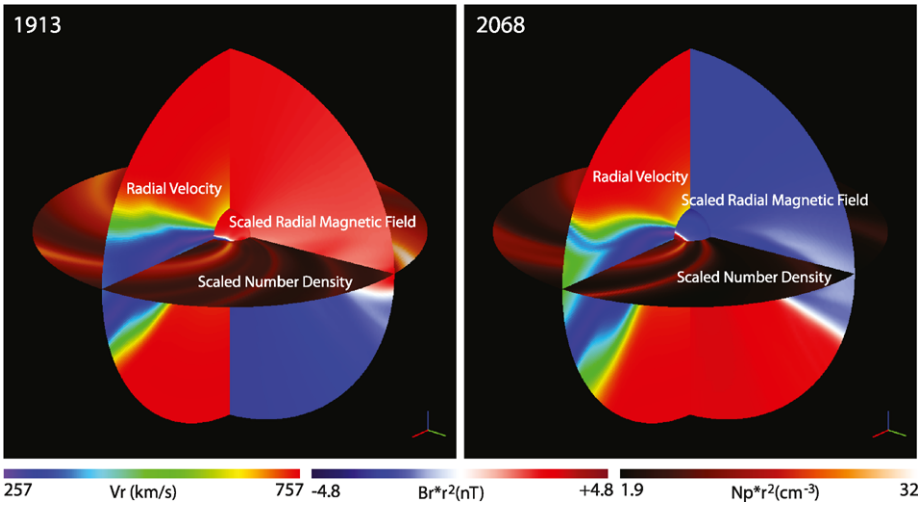

Figure 2 Illustration of the large-scale properties of the inner heliosphere (out to 1 AU) for (left) WSM and (right) WHI time periods. The two meridional slices in each panel show the radial velocity and radial magnetic-field strength, scaled to 1 AU. The slice in the equatorial plane shows the scaled number density. The sphere at $30R_{\odot}$ shows the scaled radial magnetic-field strength.

stream structure was more complex, with more interaction regions (see Gibson *et al.*, 2009, Figure 3a).

4.2. Helmet Streamer Structure

The current solar minimum, unlike the previous one, appears to have a rather unique streamer structure. Instead of the (apparently) more usual single equatorial streamer belt (that is, in coronagraph images, two streamers – one emanating from the eastern equatorial limb of the Sun and the other from the West), the streamer structure is more complex. Figure 3 shows simulation results for the WSM and WHI time periods. The model results allow us to probe the underlying magnetic structure giving rise to the observed density features in coronagraph observations.

Focusing first on CR1913, we infer that all three streamers (one on the east limb and two on the west limb) can be classified as the usual helmet streamers, where the streamer stalk marks the boundary between oppositely directed field lines, and a current sheet is associated with the interplanetary extension of this structure. However, for CR2068 we infer that, while the two streamers in the southern hemisphere, off the east and west limbs, are also helmet streamers, the two in the North are both pseudostreamers, where the field lines on either side of the streamer stalk are of the same polarity. This is further substantiated by considering the polarity of the photospheric field under the streamers. For the usual helmet streamer, one half is of one polarity and the other half is of the opposite polarity (this is clearest for the NW streamer in CR1913 and the SW streamer in CR2068), indicating that a neutral line runs through it. Finally, and most obviously, the pseudostreamers can be identified by the double-loop structure within them, which must occur if the over-arching field lines on either side have the same polarity. Wang, Sheeley, and Rich (2007) have argued that pseudostreamers are sources of fast solar wind, but our simulation results indicate that the speeds are lower in the vicinity of the pseudostreamer.

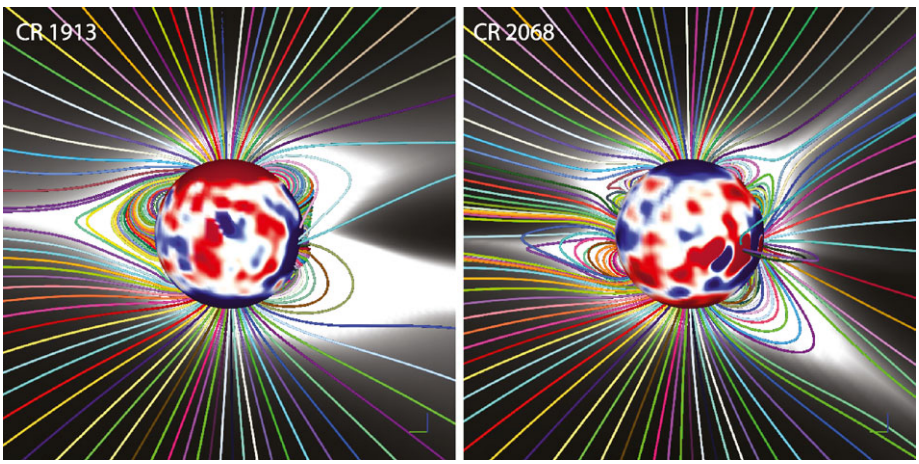

Figure 3 Composite images of the photospheric magnetic field at the solar surface (saturated at ± 1 G), with a selection of magnetic-field lines originating in the plane of the paper, and a color contour of the coronal density (scaled by r^2) for CR1913 (left) and CR2068 (right).

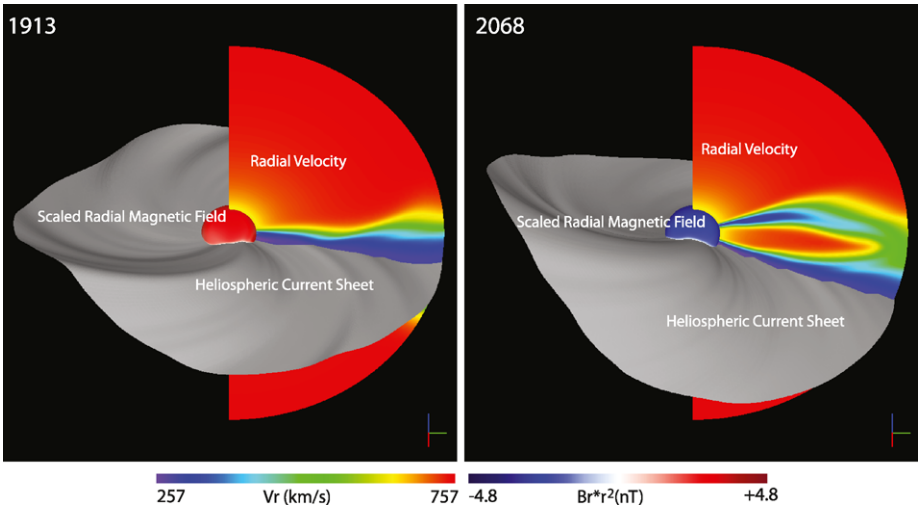

Figure 4 Illustration of the large-scale properties of the inner heliosphere (out to 1 AU) for (left) WSM and (right) WHI time periods. The isosurface marks the location of $B_r = 0$ and is the location of the HCS. The meridional slice shows radial velocity, and the sphere at $30R_\odot$ shows the radial magnetic field strength.

4.3. The Heliospheric Current Sheet

Figure 4 summarizes the shape of the HCS during the WSM and WHI time periods. Contrasting the two solutions, we note several points. First, the HCS, as well as the "band of solar wind variability," extend to higher heliographic latitudes during WHI, consistent with the results in Figure 1. Second, the polar speeds are essentially the same for the two minima. This is significant as the "self-consistent" heliospheric model was used to compute these solutions, and not the empirically based model, in which case the polar speeds would be identical by design. Instead, the similar speeds are consistent with the *Ulysses* results that while the density dropped between WSM and WHI, the speed remained constant (McComas *et al.*, 2008). Third, a significant source of fast solar wind in the ecliptic plane during WHI derives from equatorial coronal holes, whereas during WSM, the high-speed wind originated in the polar coronal holes, and, to a limited extent, from the equatorial extension of the northern polar coronal hole, known as the "elephant's trunk."

4.4. Corotating Interaction Regions

The global solar-wind structure in the heliosphere can be conveniently described by the combination of two effects. The first is that, beyond $\approx 10R_\odot$, solar material streams away from the Sun along roughly radial trajectories with a range of speeds. The second is simply that the Sun rotates: solar rotation acts to place plasma on the same radial trajectory with faster or slower wind. Faster wind overtaking slower wind leads to a compression front, while slower material being outrun by faster material leads to a rarefaction region, or expansion wave (Sarabhai, 1963). The boundary within the compression region, separating the slow and fast wind, is known as a stream interface (SI) (Gosling *et al.*, 1978). In the simplest possible scenario, where speed variations depend only on their source location at the Sun, that is, the flow pattern does not vary significantly on the time scale of a solar rotation (such as at solar minimum), the large-scale compressive structures created by the interactions of

these streams are fixed in a frame corotating with the Sun, and they are known as corotating interaction regions (CIRs, Smith and Wolfe, 1976). If the speed difference is sufficiently large, and typically beyond about 2 AU, a pair of shocks may form, bounding the CIR (*e.g.*, Pizzo, 1985).

The *Ulysses* mission revolutionized our understanding of stream structure in three dimensions. Much of the basic structure had been predicted by global MHD simulations performed by Pizzo (1991). However, it was not until *Ulysses* measurements began to uncover a systematic picture of the properties of CIRs at mid latitudes during the declining phase of Solar Cycle 22, that these earlier numerical results began to be appreciated (Pizzo and Gosling, 1994). Gosling *et al.* (1995), for example, found that CIR-associated forward shocks disappeared at helio-latitudes in excess of $\approx 26°$, which corresponded roughly to the tilt of the solar magnetic dipole. Additionally, reverse shocks continued to be observed frequently, up to latitudes of $\approx 42°$, after which their presence became rarer. Further confirmation of the model predictions came from the flow deflections observed at the shocks, suggesting that the forward shocks were oriented such that their outward normals were tilted toward the Equator, and hence were propagating equatorward, while the reverse-shock normals were tilted poleward (Riley *et al.*, 1996). These orientations can be understood heuristically based on simple geometric ideas (*e.g.*, Riley, 2010).

Figure 5 summarizes the large-scale structure of the inner heliosphere during WSM and WHI. The top panels show the three components of solar-wind velocity (in a heliocentric spherical coordinate system: r, θ, ϕ), while the bottom panels show the radial component of the magnetic field, the number density, and the plasma thermal pressure at 2.6 AU. Contrasting the two solutions, we note several points. First, the differences noted above are also present here: the "band of solar wind variability" extended to higher heliographic latitudes during CR2068; the polar speeds are essentially the same for the two minima; a significant source of fast solar wind in the ecliptic plane during CR2068 derives from equatorial coronal holes; and the computed tilt (maximum extent) of the HCS (the centroid of the white traces in the plots of radial magnetic field) matches the values shown in Figure 1. Additionally, we note that *i*) the decreases in B and B_r between CR1913 and CR2068 roughly match the changes as observed in NASA's OMNI dataset (*i.e.*, ACE and *Wind*), although the modeled values are lower than were observed (a result that is currently not understood); *ii*) the tilts of the interaction regions are much less distinct, or systematic, for CR2068 than for CR1913, although they are still present; and *iii*) during CR2068, the interaction regions are more localized and have the "U"-shaped profiles consistent with the heuristic ideas discussed by Riley, Mikić, and Linker (2003), that is, due to localized equatorial (and mid-latitude) coronal holes, "punching" through the otherwise slower wind.

5. Comparison with Observations

5.1. Extreme Ultraviolet Comparisons

As we have noted, emission images computed from the model results are quite sensitive to the form of the coronal-heating function $[H]$ used in the model. Thus, although H was not derived self-consistently from any theory of coronal heating (although it was "guided" by them), if our simulated emission matches well with observations, it suggests that our form of heating is likely a reasonable approximation to reality. In turn, it may provide a useful constraint for theories of coronal heating.

Using the densities and temperatures obtained from the global MHD models, we computed synthetic emission images in the *Extreme Ultraviolet Imaging Telescope* (EIT) bands

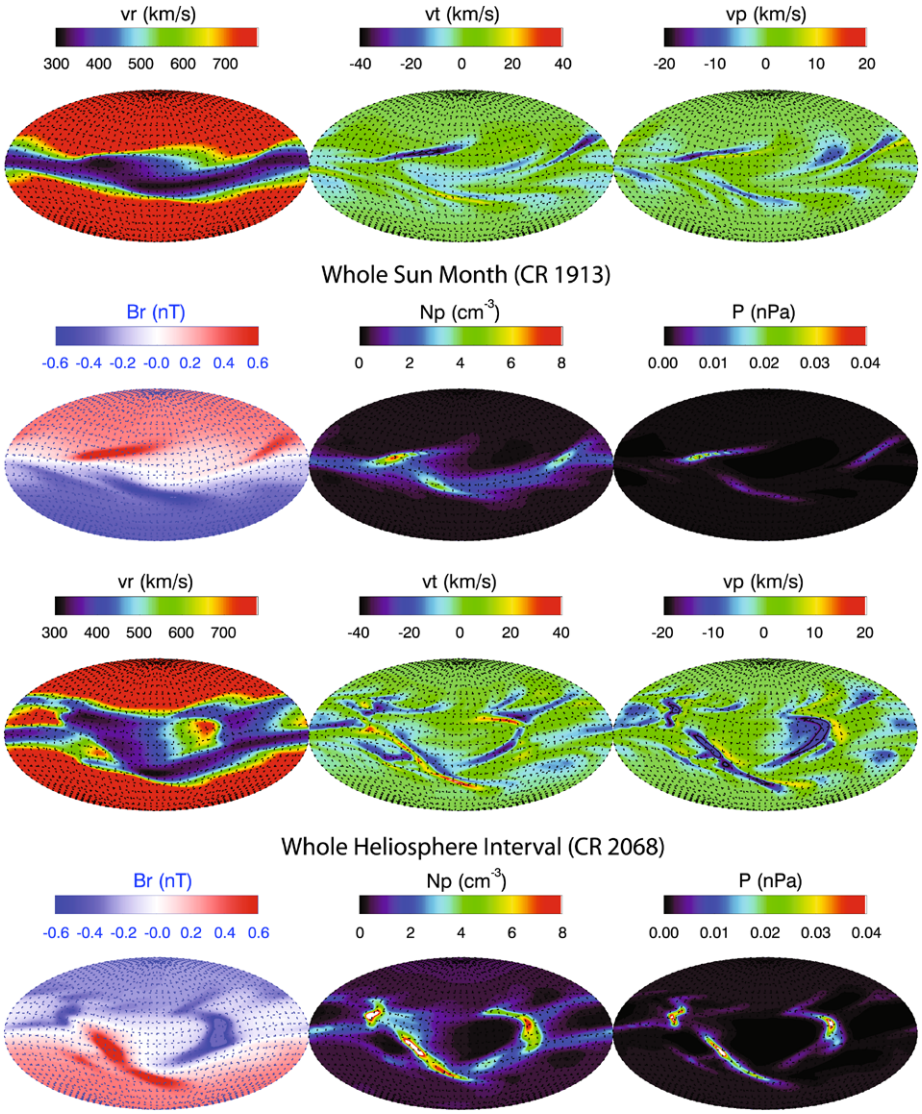

Figure 5 Mollweide projection maps of radial speed [v_r], meridional speed [v_t], azimuthal speed [v_p], radial magnetic field [B_r], scaled number density [N_p], and thermal pressure [P] for Carrington rotation 1913 (top), corresponding approximately to the Whole Sun Month (WSM) period, and 2068 (bottom), corresponding to the Whole Heliosphere Interval (WHI).

of 171, 195, and 284 Å. In Figure 6 they are compared with *Solar and Heliospheric Observatory* (SOHO)/EIT observations for CR1913. We emphasize that these are quantitative comparisons, that is, values of DN s^{-1} $pixel^{-1}$ are directly compared. We note several positive aspects of the comparison, as well as some notable discrepancies. For example, the equatorial extension of the northern polar coronal hole (the "elephant's trunk") is well reproduced in the model. Additionally, the complex AR to the East of the tip of the elephant's trunk is also captured, albeit significantly brighter than observations would suggest. Smaller

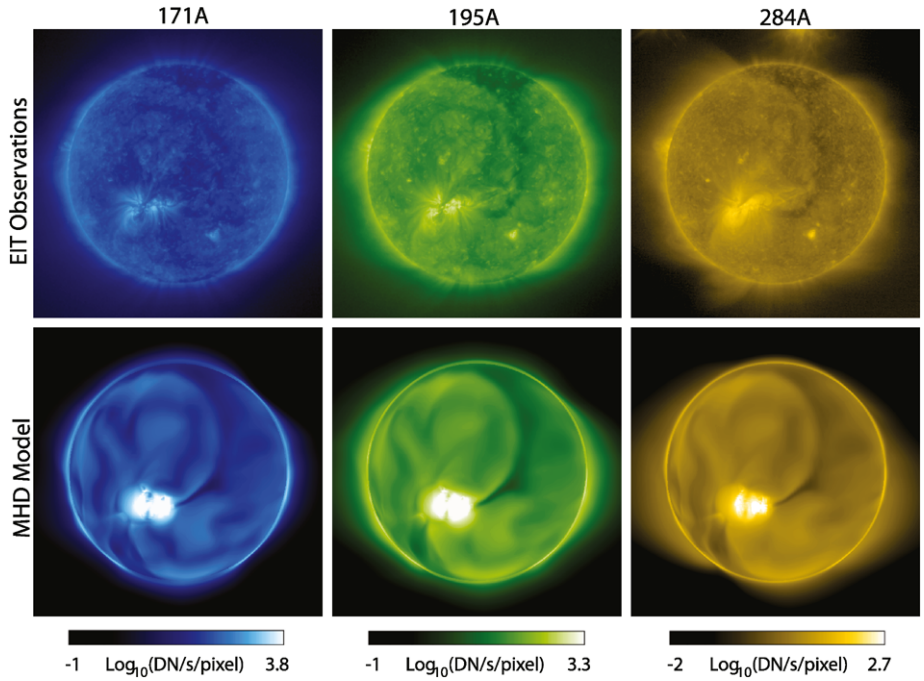

Figure 6 Comparison of SOHO/EIT emission observations at 171 Å, 195 Å, and 284 Å for Carrington rotation 1913 (top) with model results (bottom).

coronal holes, such as the one that arcs North of the AR and over to the East are also reproduced, as is the smaller one that runs away from the AR to the Southwest. Perhaps the most underappreciated match is that the overall brightness of the images, due to emission from the quiet Sun, compares favorably. The model results tend to be slightly brighter than the observations, but, overall, the close match suggests that our parameterization of the quiet-Sun heating is reasonably accurate. In identifying discrepancies, we note that some of the smaller-scale coronal hole structures in the models do not appear to have counterparts in the observations. Additionally, and not surprisingly, the model fails to pick up smaller-scale features such as the small ARs and bright points. It also does not reproduce the ray-like features emanating from the northern and southern polar coronal holes.

A comparison between simulated EIT images and observations for CR2068, using the same heating profile as for CR1913, is shown in Figure 7, and similar remarks can be made about the matches and discrepancies between the two. Unfortunately, no EIT observations at 284 Å were available at this time. One notable mismatch is that the model fails to reproduce the easternmost of the triplet of ARs. The reason may simply be that the modeled field strengths there were too low to be "lit up" by the heating function, but may also imply that our model may not be capturing important structure in the corona, which could, in turn, propagate out into significant errors in the solar wind.

5.2. *In-situ* Comparisons

While the emission image comparisons provide important information about the parameterization of the heating model, direct comparisons of model results with *in-situ* measurements

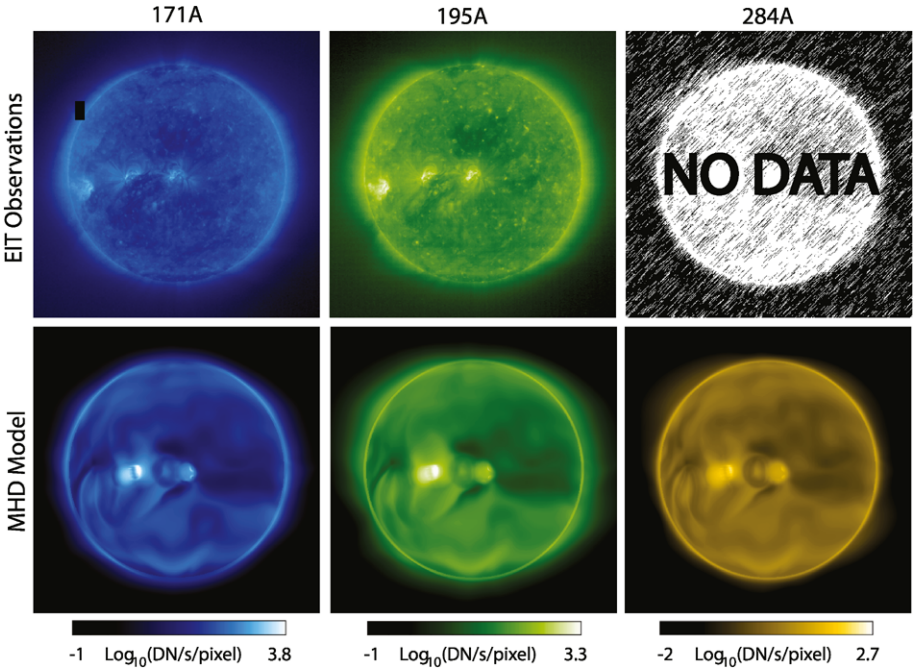

Figure 7 Comparison of SOHO/EIT emission observations at 171 Å, 195 Å, and 284 Å for Carrington rotation 2068 (top) with model results (bottom). Unfortunately, there were no data from EIT at 284 Å at this time.

provide crucial, but more difficult to interpret, feedback on a variety of model assumptions. Principally, we believe the modeled structure is most sensitive to the inner radial boundary condition for the radial component of the magnetic field: Results obtained using magnetograms from different observatories can be substantially different (*e.g.*, Riley, 2007a).

In Figure 8 we compare model results (obtained by flying the trajectory of the spacecraft through the modeling region) with observations made by the two *Solar Terrestrial Relations Observatory* (STEREO) spacecraft. We have used our simpler empirically based model (the results of which are available at http://www.predsci.com/stereo/) to illustrate how "typical" model solutions compare. Had we wanted to show the most impressive comparisons, we could have chosen to manually produce the magnetogram, and/or used magnetograms from more than six solar observatories to produce a solution that best approximates the observations. There are also several free parameters in the empirically based model used here, which, if varied, could have improved the comparison. However, our point here is to show that *i*) there is a reasonable agreement between the large-scale features in the model and observations, and *ii*) there are some noteworthy disagreements. Adjusting inputs and free parameters without understanding their role and the systematic effects on the solutions amounts to little more than "tweaking" and serves no scientific purpose, although it may be a valuable exercise in the operational environment. For more examples of comparisons, please see http://www.predsci.com/stereo/. The main points to note from Figure 8 are as follows: *i*) Overall, the model captures the two-stream flow during this time period, matching the minimum and maximum velocities. *ii*) The phasing of the fast streams between the model and observations may be offset by a day or more from one another. *iii*) The model fails to capture the sector structure of the IMF. While the sector boundary on 31 March 2008 matches

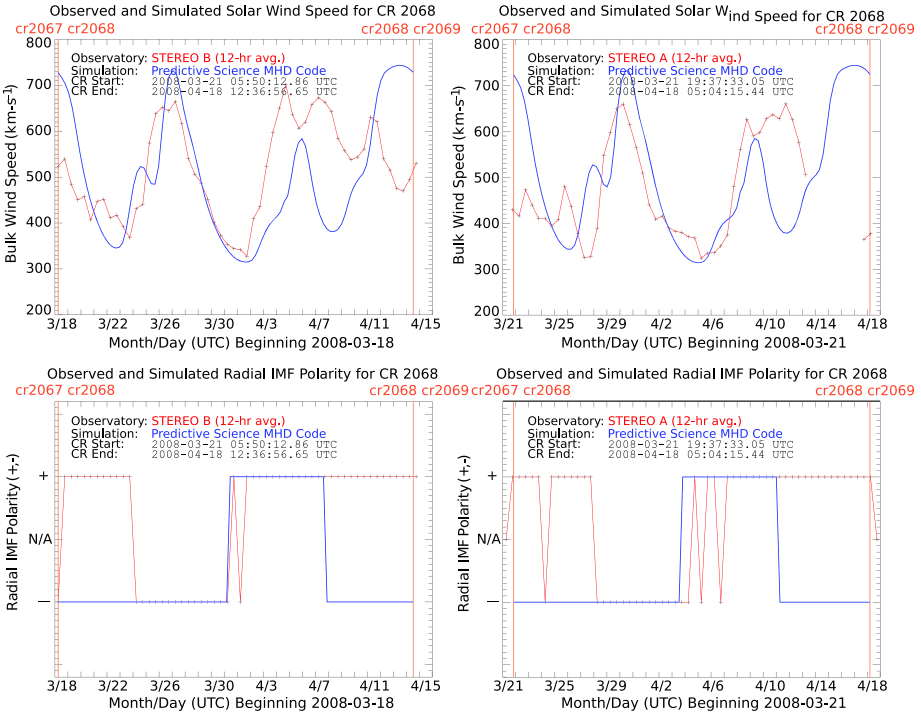

Figure 8 Time series of (top) bulk solar-wind velocity and (bottom) polarity of the radial component of the IMF. Results from STEREO-B (behind) are shown on the left and from STEREO-A (ahead) are shown on the right. Model results are colored blue, while measurements are red. The boundary of the Carrington rotation is marked by the vertical red lines.

well, the model erroneously predicts a return to negative polarity on April 2008, whereas the measurements show that this return does not occur until 24 March 2008 (since we assume that longitude [ϕ] is periodic – the solutions are in steady-state equilibrium – structures are also periodic in time).

6. Discussion and Future Directions

In this article, we have summarized our efforts to model the global structure of the solar corona and inner heliosphere during WHI. In addition to comparing the results with remote-sensing observations and *in-situ* measurements, we have contrasted the structure of the corona and heliosphere during a period approaching the recent minimum (as captured by WHI) and the previous minimum (as captured by WSM).

Overall, our modeling results have reproduced the main features of the observations, and the global picture suggested by the model has been useful in interpreting *in-situ* measurements. However, there are several significant discrepancies.

First, our *in-situ* predictions, while often reasonably accurate, are often likely to perform poorly. We are currently investigating several possible causes for this. It turns out that the model solutions are extremely sensitive to which solar observatory's magnetogram we use to drive the model (Riley *et al.*, 2011). Unfortunately, no single observatory systematically

performs better than another. Our models also contain a number of "free" parameters, the effects of which are (to varying degrees) not well known. Additionally, an intrinsic assumption of the models is that the Sun does not vary in time over the course of a solar rotation. This is clearly not the case, even during solar-minimum conditions. However, the effects of incorporating time-dependent flux evolution into these models are currently unknown.

Second, although our simulated emission images qualitatively match observations reasonably well, there are noteworthy differences. Our heating model contains a number of free (that is, not well-constrained) parameters that markedly affect the solutions. However, constructing a good set is difficult because "tuning" one parameter to affect one region on the Sun may adversely affect other regions. For example, improving emission in ARs may negatively affect the plasma properties of the resulting solar wind and/or emission in quiet-Sun regions.

In spite of these issues, we have seen significant advances in our abilities to model the corona and inner heliosphere during the nearly dozen years between WSM and WHI. Over the next decade, we anticipate commensurate advances. For example, the production of reliable chromospheric magnetograms may replace, or at least complement, the current use of photospheric magnetograms. Additionally, the incorporation of self-consistent treatments for the heating of the corona and acceleration of the solar wind (Cranmer, 2010; Rappazzo *et al.*, 2007; Buchlin and Velli, 2007; Verdini and Velli, 2007) should provide more accurate global solutions, as well as a basic test for the physics underlying these ideas. Finally, from an observational perspective, studies of STEREO remote-sensing observations and *in-situ* measurements are continuing to reveal new insights into the global properties of the inner heliosphere (*e.g.*, Riley *et al.*, 2010a). The recent launch of the *Solar Dynamics Observatory* (SDO) and the high spatial and temporal resolution of the measurements by the *Atmospheric Imaging Assembly* (AIA) and the *Helioseismic and Magnetic Imager* (HMI) will provide further, vital constraints for global models.

Acknowledgements The authors gratefully acknowledge the support of the LWS Strategic Capabilities Program (NASA, NSF, and AFOSR), the NSF Center for Integrated Space Weather Modeling (CISM), NASA's Heliophysics Theory Program (HTP), the Causes and Consequences of the Minimum of Solar Cycle 24 program, and the STEREO (IMPACT and SECCHI) teams. Data at L1 was obtained from NASA's NSSDC OMNIWEB interface. We thank J.T. Hoeksema for providing several of the parameters used to generate Figure 1. Sunspot measurements were obtained from NOAA's Space Weather Prediction Center. Simulated emission images were computed using the CHIANTI database (Dere *et al.*, 1997). Finally, we would like to thank the reviewer for useful suggestions in improving the clarity of the manuscript.

References

Athay, R.G.: 1986, Radiation loss rates in Lyman-alpha for solar conditions. *Astrophys. J.* **308**, 975 – 981. doi:10.1086/164565.

Buchlin, E., Velli, M.: 2007, Shell models of RMHD turbulence and the heating of solar coronal loops. *Astrophys. J.* **662**, 701 – 714. doi:10.1086/512765.

Cranmer, S.R.: 2010, An efficient approximation of the coronal heating rate for use in global Sun-heliosphere simulations. *Astrophys. J. Lett.* **710**, L676 – L688. doi:10.1088/0004-637X/710/1/676.

Cranmer, S.R., van Ballegooijen, A.A., Edgar, R.J.: 2007, Self-consistent coronal heating and solar wind acceleration from anisotropic magnetohydrodynamic turbulence. *Astrophys. J. Suppl. Ser.* **171**, 520 – 551. doi:10.1086/518001.

Cranmer, S.R., Kohl, J.L., Miralles, M.P., van Ballegooijen, A.A.: 2010, Extended coronal heating and solar wind acceleration over the solar cycle. In: Cranmer, S.R., Hoeksema, J.T., Kohl, J.L. (eds.) *SOHO-23: Understanding a Peculiar Solar Minimum* **CS-428**, Astron. Soc. Pacific, San Francisco, 209.

Dere, K.P., Landi, E., Mason, H.E., Monsignori Fossi, B.C., Young, P.R.: 1997, CHIANTI – an atomic database for emission lines. *Astron. Astrophys. Suppl. Ser.* **125**, 149 – 173. doi:10.1051/aas:1997368.

Emery, B.A., Richardson, I.G., Evans, D.S., Rich, F.J., Wilson, G.: 2008, Solar wind and global electron hemispheric power in solar minimum intervals. *AGU Fall Meeting Abstracts*, B1640.

Endler, F.: 1971, Wechselwirkung zwischen Sonnenwind und koronalen Magnetfeldern. *Mitt. Astron. Ges. Hamb.* **30**, 136.

Fisk, L.: 1996, Motion of the footpoints of heliospheric magnetic field lines at the sun: Implications for recurrent energetic particle events at high heliographic latitudes. *J. Geophys. Res.* **101**(A7), 15547.

Fisk, L.A., Schwadron, N.A., Zurbuchen, T.H.: 1998, On the slow solar wind. *Space Sci. Rev.* **86**, 51 – 60.

Gibson, S.E., Fludra, A., Bagenal, F., Biesecker, D., Zanna, G.D., Bromage, B.: 1999, Solar minimum streamer densities and temperatures using Whole Sun Month coordinated data sets. *J. Geophys. Res.* **104**, 9691 – 9700. doi:10.1029/98JA02681.

Gibson, S.E., Kozyra, J.U., de Toma, G., Emery, B.A., Onsager, T., Thompson, B.J.: 2009, If the Sun is so quiet, why is the Earth ringing? A comparison of two solar minimum intervals. *J. Geophys. Res.* **114**, 9105. doi:10.1029/2009JA014342.

Gosling, J.T., Asbridge, J.R., Bame, S.J., Feldman, W.C.: 1978, Solar wind stream interfaces. *J. Geophys. Res.* **83**, 1401 – 1412.

Gosling, J.T., Feldman, W.C., McComas, D.J., Phillips, J.L., Pizzo, V.J., Forsyth, R.J.: 1995, Ulysses observations of opposed tilts of solar wind corotating interaction regions in the northern and southern solar hemispheres. *Geophys. Res. Lett.* **22**(23), 3333.

Hollweg, J.V.: 1978, Some physical processes in the solar wind. *Rev. Geophys. Space Phys.* **16**, 689 – 720.

Issautier, K., Le Chat, G., Meyer-Vernet, N., Moncuquet, M., Hoang, S., MacDowall, R.J., McComas, D.J.: 2008, Electron properties of high-speed solar wind from polar coronal holes obtained by Ulysses thermal noise spectroscopy: Not so dense, not so hot. *Geophys. Res. Lett.* **35**, 19101. doi:10.1029/2008GL034912.

Jacques, S.A.: 1977, Momentum and energy transport by waves in the solar atmosphere and solar wind. *Astrophys. J.* **215**, 942 – 951. doi:10.1086/155430.

Jokipii, J.R., Sonett, C.P., Giampapa, M.S. (eds.): 1997, *Cosmic Winds and the Heliosphere*, University of Arizona, Tucson.

Kirk, M.S., Pesnell, W.D., Young, C.A., Hess Webber, S.A.: 2009, Automated detection of EUV polar coronal holes during solar cycle 23. *Solar Phys.* **257**, 99 – 112. doi:10.1007/s11207-009-9369-y.

Linker, J.A., Mikić, Z., Bisecker, D.A., Forsyth, R.J., Gibson, S.E., Lazarus, A.J., Lecinski, A., Riley, P., Szabo, A., Thompson, B.J.: 1999, Magnetohydrodynamic modeling of the solar corona during whole sun month. *J. Geophys. Res.* **104**(A5), 9809.

Lionello, R., Linker, J.A., Mikić, Z.: 2001, Including the transition region in models of the large-scale solar corona. *Astrophys. J.* **546**, 542.

Lionello, R., Linker, J.A., Mikić, Z.: 2009, Multispectral emission of the Sun during the first whole Sun month: Magnetohydrodynamic simulations. *Astrophys. J.* **690**, 902 – 912. doi:10.1088/0004-637X/690/1/902.

Manchester, W.B., Ridley, A.J., Gombosi, T.I., Dezeeuw, D.L.: 2006, Modeling the Sun-to-Earth propagation of a very fast CME. *Adv. Space Res.* **38**, 253 – 262. doi:10.1016/j.asr.2005.09.044.

McComas, D.J., Ebert, R.W., Elliott, H.A., Goldstein, B.E., Gosling, J.T., Schwadron, N.A., Skoug, R.M.: 2008, Weaker solar wind from the polar coronal holes and the whole Sun. *Geophys. Res. Lett.* **35**, 18103. doi:10.1029/2008GL034896.

Mikić, Z., Linker, J.A.: 1994, Disruption of coronal magnetic field arcades. *Astrophys. J.* **430**, 898.

Mikić, Z., Linker, J.A., Schnack, D.D., Lionello, R., Tarditi, A.: 1999, Magnetohydrodynamic modeling of the global solar corona. *Phys. Plasmas* **6**(5), 2217.

Odstrcil, D.: 1994, Interactions of solar wind streams and related small structures. *J. Geophys. Res.* **99**(A9), 17653.

Odstrcil, D., Pizzo, V.J., Linker, J.A., Riley, P., Lionello, R., Mikic, Z.: 2004, Initial coupling of coronal and heliospheric numerical magnetohydrodynamic codes. *J. Atmos. Solar-Terr. Phys.* **66**, 1311 – 1320.

Phillips, T.: 2009, Science at NASA: Deep solar minimum. http://science.nasa.gov/science-news/science-at-nasa/2009/01apr_deepsolarminimum/.

Pizzo, V.: 1978, A three-dimensional model of corotating streams in the solar wind. I – Theoretical foundations. *J. Geophys. Res.* **83**, 5563 – 5572.

Pizzo, V.J.: 1985, Interplanetary shocks on the large scale: A retrospective on the last decade's theoretical efforts. *Collisionless Shocks in the Heliosphere: Rev. Curr. Res.* **35**(A87-25331 09-92), 51.

Pizzo, V.J.: 1991, The evolution of corotating stream fronts near the ecliptic plane in the inner solar system. II – Three-dimensional tilted-dipole fronts. *J. Geophys. Res.* **96**, 5405 – 5420.
Pizzo, V.J., Gosling, J.T.: 1994, 3-D simulation of high-latitude interaction regions: Comparison with Ulysses results. *Geophys. Res. Lett.* **21**(18), 2063.
Pneuman, G.W., Kopp, R.A.: 1971, Gas-magnetic field interactions in the solar corona. *Solar Phys.* **18**, 258.
Rappazzo, A.F., Velli, M., Einaudi, G., Dahlburg, R.B.: 2007, Coronal heating, weak MHD turbulence, and scaling laws. *Astrophys. J. Lett.* **657**, L47 – L51. doi:10.1086/512975.
Riley, P.: 2007a, An alternative interpretation of the relationship between the inferred open solar flux and the interplanetary magnetic field. *Astrophys. J. Lett.* **667**, L97 – L100. doi:10.1086/522001.
Riley, P.: 2007b, Modeling corotating interaction regions: From the Sun to 1 AU. *J. Atmos. Solar-Terr. Phys.* **69**, 32 – 42. doi:10.1016/j.jastp.2006.06.008.
Riley, P.: 2010, The three-dimensional structure of the inner heliosphere. In: Maksimovic, M., Meyer-Vernet, N., Moncuquet, M., Pantellini, F. (eds.) *Twelfth International Solar Wind Conference AIP* **CS-1216**, 323 – 328. doi:10.1063/1.3395865.
Riley, P., McComas, D.J.: 2009, Derivation of fluid conservation relations to infer near-Sun properties of coronal mass ejections from in situ measurements. *J. Geophys. Res.* **114**, 9102. doi:10.1029/2009JA014436.
Riley, P., Linker, J.A., Mikić, Z.: 2001, An empirically-driven global MHD model of the corona and inner heliosphere. *J. Geophys. Res.* **106**(A8), 15889.
Riley, P., Linker, J.A., Mikić, Z.: 2002, Modeling the heliospheric current sheet: Solar cycle variations. *J. Geophys. Res.* **107**(A7). doi:1010292001JA000299.
Riley, P., Mikić, Z., Linker, J.A.: 2003, Dynamical evolution of the inner heliosphere approaching solar activity maximum: Interpreting Ulysses observations using a global MHD model. *Ann. Geophys.* **21**, 1347.
Riley, P., Gosling, J.T., Weiss, L.A., Pizzo, V.J.: 1996, The tilts of corotating interaction regions at midheliographic latitudes. *J. Geophys. Res.* **101**(A11), 24349.
Riley, P., Gosling, J.T., McComas, D.J., Pizzo, V.J., Luhmann, J.G., Biesecker, D., Forsyth, R.J., Hoeksema, J.T., Lecinski, A., Thompson, B.J.: 1999, Relationship between Ulysses plasma observations and solar observations during the whole Sun month campaign. *J. Geophys. Res.* **104**(A5), 9871.
Riley, P., Linker, J.A., Mikić, Z., Lionello, R.: 2001, MHD modeling of the solar corona and inner heliosphere: Comparison with observations. In: Song, P., Singer, H.J., Siscoe, G.L. (eds.) *Space Weather, Geophysical Monograph Series* **125**, AGU, Washington, 159.
Riley, P., Lionello, R., Mikić, Z., Linker, J., Clark, E., Lin, J., Ko, Y.K.: 2007, "Bursty" reconnection following solar eruptions: MHD simulations and comparison with observations. *Astrophys. J.* **655**, 591 – 597. doi:10.1086/509913.
Riley, P., Luhmann, J., Opitz, A., Linker, J.A., Mikic, Z.: 2010a, Interpretation of the cross-correlation function of ACE and STEREO solar wind velocities using a global MHD model. *J. Geophys. Res. (Space Phys.)* **115**, 11104. doi:10.1029/2010JA015717.
Riley, P., Mikic, Z., Lionello, R., Linker, J.A., Schwadron, N.A., McComas, D.J.: 2010b, On the relationship between coronal heating, magnetic flux, and the density of the solar wind. *J. Geophys. Res.* **115**, 6104. doi:10.1029/2009JA015131.
Riley, P., Mikic, Z., Linker, J.A., Harvey, J., Hoeksema, T., Liu, Y., Ulrich, R., Bertello, L.: 2011, A multi-observatory inter-calibration of line-of-sight diachronic solar magnetograms and implications for the open flux of the heliosphere. *Astrophys. J.*, submitted.
Roussev, I.I., Gombosi, T.I., Sokolov, I.V., Velli, M., Manchester, W., DeZeeuw, D.L., Liewer, P., Tóth, G., Luhmann, J.: 2003, A three-dimensional model of the solar wind incorporating solar magnetogram observations. *Astrophys. J. Lett.* **595**, L57 – L61.
Sarabhai, V.: 1963, Some consequences of nonuniformity of solar wind velocity. *J. Geophys. Res.* **68**, 1555.
Smith, E.J., Balogh, A.: 2008, Decrease in heliospheric magnetic flux in this solar minimum: Recent Ulysses magnetic field observations. *Geophys. Res. Lett.* **35**, 22103. doi:10.1029/2008GL035345.
Smith, E.J., Wolfe, J.H.: 1976, Observations of interaction regions and corotating shocks between one and five AU: Pioneers 10 and 11. *Geophys. Res. Lett.* **3**, 137.
Svalgaard, L., Cliver, E.W.: 2007, A floor in the solar wind magnetic field. *Astrophys. J. Lett.* **661**, L203 – L206. doi:10.1086/518786.
Verdini, A., Velli, M.: 2007, Alfvén waves and turbulence in the solar atmosphere and solar wind. *Astrophys. J.* **662**, 669 – 676. doi:10.1086/510710.
Wang, Y.M., Sheeley, N.R. Jr.: 1990, Solar wind speed and coronal flux-tube expansion. *Astrophys. J.* **355**, 726.
Wang, Y.M., Sheeley, N.R. Jr., Rich, N.B.: 2007, Coronal pseudostreamers. *Astrophys. J.* **658**, 1340 – 1348. doi:10.1086/511416.